JOURNAL OF AIRCRAFT
Vol. 46, No. 2, March–April 2009

Propulsive Force of a Flexible Flapping Thin Airfoil

U. Gulcat*
Istanbul Technical University, 34469 Istanbul, Turkey

DOI: 10.2514/1.35310

The propulsive force generated by the leading-edge suction of a flapping thin airfoil can be obtained using unsteady aerodynamic notions based on the potential flow theory. Because the potential theory fails to predict the viscous forces, for flapping airfoils, in general there exists a net propulsive force generation. For low Reynolds numbers and for oscillations at low reduced frequencies, however, the viscous forces overcome the propulsive forces to give a net force against the flight direction. In the case of higher Reynolds numbers, flappings with large amplitudes, and high frequencies, the leading-edge suction force generated by the airfoil overcomes the viscous forces. In this study, the critical Reynolds number, the amplitude, and the reduced frequency values that yield the net propulsive force for an oscillating airfoil are predicted with unsteady viscous–inviscid interaction. The airfoil motions are modeled as 1) a thin rigid plate in vertical oscillation, that is, a heaving–plunging motion; 2) a flexibly cambered airfoil whose camber is changing periodically; and 3) the heaving–plunging motion of a flexibly cambered airfoil. The leading-edge suction force for all cases is predicted by means of the well-known Blasius theorem, and the time dependent surface velocity distribution of the airfoil is determined by unsteady aerodynamic considerations. This surface velocity distribution is used as the edge velocity of the unsteady boundary layer to predict the viscous effects. The coefficient of the propulsive force predicted with the present method agrees well with the values given in the literature up to the effective angle of attack at which the dynamic stall takes place.

Nomenclature

a	=	airfoil camber
a^*	=	maximum camber
b	=	half chord
C	=	chord
$C(k)$	=	Theodorsen function, $F(k) + iG(k)$
C_p	=	pressure coefficient
C_{Tid}	=	ideal averaged force coefficient
c_d	=	drag force coefficient
c_F	=	propulsive force coefficient
c_f	=	skin friction coefficient
c_s	=	suction force coefficient
c_T	=	averaged propulsive force coefficient
h	=	heaving–plunging parameter
h^*	=	dimensionless amplitude
i	=	index in the x direction
j	=	index in the y direction
n	=	index in time
Re	=	Reynolds number
k	=	reduced frequency
S	=	leading-edge suction force
s	=	reduced time
U	=	freestream velocity
U_e	=	edge velocity
u	=	horizontal component of velocity
v	=	vertical component of velocity in the viscous region
w	=	downwash
z_a	=	camber equation
α	=	angle of attack
α_d	=	dynamic stall angle
α_e	=	effective angle of attack
Γ_a	=	bound vortex
γ_a	=	surface vortex sheet strength
γ_w	=	wake vortex sheet strength
Δt	=	time step
Δx	=	step in the x direction
Δy	=	step in the y direction
δ	=	boundary-layer thickness
ν	=	kinematic viscosity
ρ	=	density of the air
ω	=	vorticity, angular frequency
ω_o	=	surface vorticity

I. Introduction

THE concept of creating a propulsive force with flapping wings, undoubtedly, is derived from the examples existing in nature for hundreds of millions of years [1,2]. In recent decades, this concept has been widely exploited because of the continuing increase in demand for the aerodynamic design of micro air vehicles (MAVs) [3,4]. The aerodynamic forces generated by the heaving–plunging motion of a thin airfoil submerged in a freestream can be obtained by means of the famous Blasius theorem [5], whose extended versions can be found in [6,7]. The aerodynamic force generated in the direction normal to the flight is the lifting force. The force created in the direction of the flight while flapping is due to the leading-edge suction, and it is responsible for sustaining the forward flight. The unsteady aerodynamic considerations, on the other hand, tell us that the aerodynamic response of an airfoil to an unsteady motion has a certain phase lag and amplitude reduction for the forces and the moments. The measure of this phase lag and the amplitude reduction are given by a complex function called the Theodorsen function [8]. It is the property of the Theodorsen function that, with increasing frequency, the phase lag and the amplitude reduction also increase. In addition, for higher frequency values, the apparent mass term becomes high and creates a significant noncirculatory lifting force that has a 90 deg phase lag with the airfoil motion.

For heaving–plunging airfoils, the unsteady potential theory predicts a propelling force for the entire range of reduced frequency k [7]. In real life, however, there is always a drag force that consists of skin friction and the form drags against the propelling force. The value of the flapping frequency and its amplitude play an important role for the propulsive force in overcoming the drag force [4]. It is shown in this study that the Reynolds number also plays a critical part in that role in obtaining a net propulsive force. In that respect, below the critical values, the viscous forces overcome the leading-edge

Received 26 October 2007; revision received 25 November 2008; accepted for publication 25 November 2008.

*Emeritus Professor, Faculty of Aeronautics and Astronautics.

suction force; therefore, the very idea of the generation of a propulsive force with wing flapping fails. In this study, using the concept of the viscous–inviscid coupling, a series of solutions are obtained to predict the lower bounds for flapping frequency, amplitude, and the Reynolds number, which gives a net propulsive force. In this context, the unsteady boundary-layer equations are solved numerically with a method similar to that given in [9,10] to predict the viscous effects on the oscillating thin airfoil. The boundary-layer theory gives meaningful results only for the attached flow regions. The flow separation prevents the further application of the boundary-layer concept. The flow separation may occur at low angles of attack for static stall cases [11]. For the case of dynamic stall, however, the separation occurs at higher angles with the increase of flapping frequency [12]. Therefore, the boundary-layer theory remains applicable for a wide range of angles of attack. During the last decade, the full Navier–Stokes equations were employed as computational fluid dynamics tools to study the flapping airfoil problem [13], for which very fine time and space resolutions are demanded. The viscous–inviscid coupling approach, however, needs comparably less computational time while giving agreeable results with those of [13] before the dynamic stall occurrence. The demand for computer time and storage increases much more when performing meaningful parametric studies for the computation of the time-dependent aerodynamic coefficients with deforming grids for flexible airfoil flapping. The current status of the research on flexible airfoil flapping is provided in [4].

In this study, three different types of flapping motion of a thin airfoil to obtain net propulsive force will be considered. First, the heaving–plunging of a rigid airfoil will be studied for calibration purposes. After calibration, the propulsive force generated by the periodic changing of a camber of a flexible airfoil and the heaving–plunging of a flexibly cambered airfoil will be considered as the second and third cases, respectively. For both studies, the leading-edge suction force as well as the edge velocity for the unsteady boundary layer will be provided from the unsteady potential theory. In the following sections, the theoretical as well as the numerical formulation based on the velocity–vorticity formulation for determining the skin friction will be given. The comparison of the results with the existing literature will be discussed. Finally, the conclusions based on the numerical results obtained will be provided.

II. Formulation

The formulas for the theoretical evaluation of leading-edge suction forces for a thin airfoil heaving plunging in a free stream (Sec. II.A) with a flexible camber that changes periodically (Sec. II.B) and the simultaneous motion given with these two (Sec. II.C) are derived from the unsteady aerodynamic considerations.

A. Heaving–Plunging Airfoil

The sectional propulsive force S, created by the leading-edge suction of a vertically oscillating airfoil, is given by

$$S = -2\rho\pi[\dot{h}C(k)]^2 \tag{1}$$

Here, $h = -h^* \cos(\omega t)$ is the time variation of the height of the vertical oscillation, $\dot{}$ denotes the derivative with respect to time, and $C(k)$ is the Theodorsen function whose real part is given by $F(k)$ and imaginary part is given by $G(k)$, where $k = \omega b/U$ is the reduced frequency [8]. The derivation of Eq. (1) is given in the Appendix via Eqs. (A3), (A4), and (A7). If we denote the reduced time by $s = Ut/b$, wherein b is the half-chord, then the coefficient of the sectional propulsive force reads

$$c_s = S/(\rho U^2 b) = -2\pi k^2[G(k)\cos(ks) + F(k)\sin(ks)]^2 \bar{h}^{*2} \tag{2}$$

wherein $\bar{h}^* = h^*/b$ is the nondimensional amplitude of the vertical oscillation. Figure 1 shows all the parameters involved in the oscillation, the bound vortex Γ_a, and the vortex sheet strength at the wake γ_w.

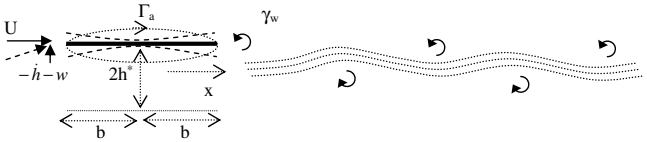

Fig. 1 The vertically oscillating flexible airfoil and its wake region.

The corresponding nondimensional surface velocity distribution for the airfoil is obtained from Eq. (A8) of the Appendix, as follows:

$$U_e(s)/U = 1 \pm [F(k)\sin(ks) + G(k)\cos(ks)]k\bar{h}^* \sqrt{(1-x)/(1+x)} \tag{3}$$

where $+$ stands for the upper surface, $-$ stands for the lower surface, and x is the nondimensional surface coordinate running between -1 and $+1$. Equation (3) is obtained via the normalization of Eq. (A8) of the Appendix.

B. Airfoil with a Flexible Camber

In this case, the thin airfoil is represented with a camber line whose equation, for simplicity, is given as

$$z_a(x,t) = -a(t)x^2/b^2, \qquad a(t) = a^* \cos(\omega t)$$

Here, a^* is the amplitude of the parabolically varying camber geometry of the airfoil as shown by the dashed lines in Fig. 1. The sectional suction force coefficient for the cambered airfoil using Eqs. (A3), (A4), and (A11) reads as

$$c_s = -2\pi[(F - 1 - Gk/2)\cos(ks) - (G + Fk/2\sin(ks))]^2 \bar{a}^{*2} \tag{4}$$

The corresponding surface velocity distribution this time is given by Eq. (A12) as

$$\frac{U_e}{U} = 1 \pm \{[(1 + 2x + F) - Gk/2]\cos ks - [(G + (x + x^2 + F/2)k]\sin ks\}\bar{a}^* \sqrt{\frac{1-x}{1+x}} \tag{5}$$

wherein $\bar{a}^* = a^*/b$ is the nondimensional amplitude of the camber.

The surface velocity distributions given by Eqs. (3) and (5) are used as the edge velocities for the unsteady boundary layer whose equations are going to be provided in the next section.

C. Heaving–Plunging Airfoil with a Flexible Camber

The suction force is obtained with Eqs. (2) and (4) and the edge velocity is provided by Eqs. (3) and (5) combined.

III. Boundary-Layer Equations

As is well known, the boundary-layer equations are obtained from the Navier–Stokes equations through some simplifying assumptions based on the fact that there is no flow separation from the surface of the airfoil [14]. Another assumption is that the order of the terms in the main flow direction and the gradients perpendicular to the surface are always high and, therefore, cannot be neglected. The pressure gradient term on the boundary-layer equations is imposed from the potential flow. However, there is a more convenient form of the boundary-layer equations in which the pressure term does not appear explicitly if they are expressed in a velocity–vorticity formulation. Furthermore, with the velocity–vorticity formulation, the equations cast in moving–deforming coordinates attached to the airfoil take a simple form if there is only rigid body translation [15] and/or if there is a negligible rotation in movements involving flexibility. The finite difference discretization of the boundary-layer equations, on the other hand, is made in such a way that at a given time level the vorticity values are obtained implicitly from the x component of the momentum equation while marching from station to station. At each

station, from the definition of vorticity, the u component of the velocity is calculated by integration and the continuity equation is solved explicitly to obtain the v component of the velocity vector. The velocity–vorticity formulation of the boundary-layer equations and the numerical formulation for the discretization are provided in Secs. III.A and III.B, respectively.

A. Velocity–Vorticity Formulation

The definition of the vorticity vector $\boldsymbol{\omega} = \nabla \wedge \mathbf{v}$ from the velocity field $\mathbf{v}$ in two dimensions gives the equations for the velocity–vorticity formulation expressed in body-fixed coordinates [15] as follows:

$$\nabla . \mathbf{v} = 0 \tag{6}$$

$$\frac{\mathrm{D}\omega}{\mathrm{D}t} = \nu \nabla^2 \omega \tag{7}$$

Here, ω is the z component of the vorticity vector expressed in the inertial frame of reference. The open and nondimensional forms of Eqs. (6) and (7) simplify for the boundary-layer flows about flexible airfoils as obtained in the Appendix with Eq. (A18) to become

$$\frac{\partial u}{\partial x} + \frac{\partial v}{\partial y} = 0 \tag{8}$$

and

$$\frac{\partial \omega}{\partial t} + u \frac{\partial \omega}{\partial x} + v \frac{\partial \omega}{\partial y} = \frac{1}{\mathrm{Re}} \frac{\partial^2 \omega}{\partial y^2} \tag{9}$$

wherein all independent and dependent variables are made nondimensional with respect to the freestream speed U and the chord c. Re is the Reynolds number based on the freestream speed, the chord, and the kinematic viscosity. Furthermore, using the boundary-layer concept, one can simplify the definition of vorticity to read

$$\omega = -\frac{\partial u}{\partial y} \tag{10}$$

which will be used in evaluating the u component of the velocity by integrating the vorticity values at a given station. Another useful expression is the thin airfoil surface skin friction formula, which in nondimensional form reads as the sectional skin friction coefficient:

$$c_f = -\frac{2}{Re} \omega_o \tag{11}$$

where ω_o is the surface vorticity value measured in the inertial frame of reference. The integral of Eq. (11) along the upper and lower surfaces gives the viscous drag coefficient, c_d, opposing the propulsive force.

B. Numerical Formulation

The boundary-layer equations given in Sec. III.A are discretized with finite differencing. Accordingly, Eq. (9) is discretized on a Cartesian grid with finite steps of Δt in time and Δx and Δy in space. If we use forward differencing in time and in the x directions, and central differencing in the y direction, the discretized form of Eq. (9) then reads as

$$\frac{\omega_{i,j}^n - \omega_{i,j}^{n-1}}{\Delta t} = -u_{i,j}^{n-1} \frac{\omega_{i,j}^n - \omega_{i-1,j}^n}{\Delta x} - v_{i,j}^{n-1} \frac{\omega_{i,j+1}^n - \omega_{i,j-1}^n}{2\Delta y} + \frac{1}{\mathrm{Re}} \frac{\omega_{i,j+1}^n - 2\omega_{i,j}^n + \omega_{i,j-1}^n}{(\Delta y)^2} \tag{12}$$

where the superscript n denotes the new time level, and subscripts i and j denote the discrete point in x and y, respectively. To solve Eq. (12) for the new time level n at a given station i, the vorticity values at the surface and the edge of the boundary layer must be known. The edge vorticity along the boundary layer at the last point J is set to $\omega_{i,J} = 0$, and the surface vorticity $\omega_{i,o}$ is calculated with the numerical integration of Eq. (10) using the trapezoidal rule at a station i with respect to y as follows:

$$U_e|_i = -\int_0^\delta \omega \, \mathrm{d}y|_i = -\left[\omega_{i,o}/2 + \sum_{j=1}^{J-1} \omega_{i,j}\right] \Delta y \tag{13}$$

Rearranging Eqs. (12) and (13) and casting the result in matrix form, with Eq. (13) being the first row, we obtain

$$\begin{bmatrix} 1/2 & 1 & 1 & . & 1 \\ a_2 & d_2 & c_2 & . & . \\ . & a_3 & d_3 & c_3 & . \\ . & . & . & . & . \\ . & . & . & a_j & d_j \end{bmatrix} \begin{pmatrix} \omega_{i,o} \\ \omega_{i,1} \\ \omega_{i,2} \\ . \\ \omega_{i,J-1} \end{pmatrix}^n = \begin{pmatrix} -U_e/\Delta y \\ b_2 \\ b_3 \\ . \\ b_J \end{pmatrix}_i^n \tag{14}$$

Here, Eq. (14) contains the vorticity values as unknowns that are, at a given station, as many as J, and the elements of the coefficient matrix and the right-hand side vector are known from the old time level values of the velocity and vorticity field except U_e, which is provided by Eq. (3) or Eq. (5) at a new time level. These values, for $j = 2, \ldots, J$, read

$$a_j = -v_{i,j-1}^{n-1} \frac{\Delta t}{2\Delta y} - \frac{\Delta t}{R_e \Delta y^2}, \qquad c_j = v_{i,j+1}^{n-1} \frac{\Delta t}{2\Delta y} - \frac{\Delta t}{R_e \Delta y^2}$$

$$b_j = \omega_{i,j}^{n-1} + u_{i,j}^{n-1} \omega_{i-1,j}^n \frac{\Delta t}{\Delta x}, \qquad d_j = 1 + u_{i,j}^{n-1} \frac{\Delta t}{\Delta x} + \frac{2\Delta t}{R_e \Delta y^2}$$

Equation (14) is a tridiagonal matrix equation except in the first row. The direct inversion of Eq. (14) is made with the Sherman–Morison formula [16] to calculate the vorticity values at any station. Once the vorticity values are determined at the station i, the u component of the velocity at a discrete point i, j is obtained by integrating Eq. (10) as follows:

$$u_{i,j} = -\int_0^{y_j} \omega \, \mathrm{d}y|_i = -\left[\sum_{m=1}^{j-1} (\omega_{i,m-1} + \omega_{i,m})/2\right] \Delta y \qquad j = 2, \ldots, J \tag{15}$$

So far, at a station i along the boundary layer, the vorticity and the u component of the velocity values are determined. To complete the marching process, the v component of the velocity is computed from the continuity equation, Eq. (8), as follows:

$$v_{i,j}^n = v_{i,j-1}^n - \frac{\Delta y}{2\Delta x} (u_{i,j} + u_{i,j-1} - u_{i-1,j} - u_{i-1,j-1})^n, \qquad j = 2, J \tag{16}$$

To obtain the expression given with Eq. (16), the averaged u values u_L and u_R, as shown in Fig. 2, are used for the numerical differentiation in the x direction, that is, $\partial u/\partial x = (u_R - u_L)/\Delta x$, and $\partial v/\partial y = (v_{i,j} - v_{i,j-1})/\Delta y$ in the y direction. The grid points involved in the discretization of the continuity equation, Eq. (8), at point $i, j - \frac{1}{2}$, are shown in detail in Fig. 2.

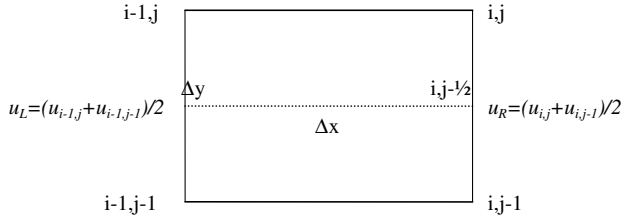

Fig. 2 Discretization for the continuity equation at point $i, j - \frac{1}{2}$, mesh size Δx and Δy.

IV. Solution Procedure

The net propulsive force of an oscillating thin rigid or flexible airfoil is calculated using the equations given in Secs. II and III in the following steps in which the unsteady aerodynamic viscous–inviscid coupling is considered.

1) The time-dependent suction force coefficients, c_s, are calculated with Eq. (2) and/or Eq. (4).

2) The time-dependent edge velocity, U_e, is computed with Eq. (3) and/or Eq. (5).

3) At a given time level n and for a station i along the boundary layer, the vorticity values are computed by solving Eq. (14) with the known values of the edge velocity and the other relevant parameters.

4) The velocity components u and v at a station i are calculated with Eqs. (15) and (16), respectively.

5) The surface skin friction coefficient at the station i is computed with Eq. (11).

6) The solution is marched stationwise in i for the time level n.

7) The integral of the surface skin friction coefficient, found in step 5, along the surface gives the drag, c_d.

8) The net propulsive force coefficient at the time level n is calculated as the difference between the suction force coefficient found in step 1 and the drag force coefficient in step 7.

9) Steps 3–8 are repeated until the desired number of oscillations are achieved,

10) Finally, the time averaged value of the propulsive force coefficient, c_T, is obtained by the timewise integration of the result found in step 8 over a representative time period.

V. Results and Discussion

The solution procedure described in Sec. IV based on the viscous–inviscid interaction is first tested to determine the net propulsive force created by a heaving–plunging thin airfoil. After the calibration, the procedure is first applied to obtain the propulsive force of a flexible cambered airfoil that has only its camber amplitude periodically changing in time and then applied to study the motion of an airfoil for which the heaving plunging and the camber flexibility are combined.

A. Heaving–Plunging Airfoil

The heaving–plunging airfoil in a freestream of U has the periodic vertical motion given with

$$h = -h^* \cos(\omega t) \tag{17}$$

The sectional suction force given by Eq. (2) and the drag force obtained by the integration of the skin friction coefficient, Eq. (11) together give the time variation of net propulsive force coefficient. The timewise integration of the net propulsive force coefficient over a representative time period, on the other hand, provides us with the average propulsive force produced by the oscillation. During the vertical oscillation given by Eq. (17) in a freestream U, the relative vertical air velocity component reads as $-\dot{h}$. This results in an effective angle of attack, α_e, which is experienced by the airfoil, as follows:

$$\alpha_e = \tan^{-}(-\dot{h}/U_\infty) \tag{18}$$

As mentioned before, in order for the viscous–inviscid interaction approach to be valid for the external flows, there should not be a flow separation. Therefore, one has to be cautious about a critical angle of attack beyond which the flow separates and causes airfoil to stall. It is also known that for the same airfoil the static stall occurs at lower angles of attack than the dynamic stall depending on the reduced frequency k of the oscillations. The relation between the angles for static stall α_s and the dynamic stall α_d is given in [12] as follows:

$$\alpha_d = \alpha_s + \Delta\alpha = \alpha_s + 0.3\sqrt{k}(180/\pi) \tag{19}$$

For example, the static stall angle of attack for the NACA 0012 is 12 deg and, if it is oscillating with the reduced frequency $k = 0.4$, the dynamic stall angle of attack, according to Eq. (19), then becomes

$$\alpha_d = 12 \text{ deg} + 0.3\sqrt{k}(180/\pi) = 12 \text{ deg} + 10.88 \cong 23 \text{ deg} \tag{20}$$

The angle obtained with Eq. (20), therefore, dictates that the effective angle of attack α_e, given with Eq. (18), should be less then 23 deg in order for the flow around the NACA 0012 not to separate. If we insist on using viscous–inviscid interaction approach for the separated flow case, then the propulsive force coefficients will be overestimated. This fact was observed during the calibration studies made for the NACA 0012 airfoil heaving plunging with a reduced frequency of $k = 0.4$ and a Reynolds number of 10^5. The comparison of the results with [13], for various dimensionless amplitudes $\bar{h}^* = h^*/b$, are given in Table 1.

According to Table 1, the averaged propulsive force coefficient computed with the present method overestimates the values when compared with [13], in which a full Navier–Stokes solver is employed. The reason for this overestimation, almost 10% for $\bar{h}^* = 0.8$ and 1.0, before the occurrence of dynamic stall, is mainly the effect of the form drag, which is neglected because of thin airfoil assumption. The overestimation, on the other hand, is more than 100% for the case of $\bar{h}^* = 1.2$, in which the effective angle of attack, $\alpha_e = 25$ deg, is greater than the $\alpha_d = 23$ deg dynamic stall angle, which means the flow has separated and there is a definite loss in the propulsive force generated by flapping. Also given in Table 1 are the corrected C_T values for the NACA 0012 airfoil. The corrections are made for the thickness effect on the edge velocity and are based on the theory given by [17]. The corrected C_T values indicate that, for the low effective angles of attack, the agreement with the Navier–Stokes solution is very good.

After the calibration, various parametric studies are performed for the heaving–plunging airfoil to determine the effect of the reduced frequency of oscillation, the amplitude, and the Reynolds number on the propulsive force before the occurrence of dynamic stall. The variation of the averaged propulsive force coefficient, c_T, for different amplitudes of $\bar{h}^* = 0.2$, 0.4, and 0.6 is given in Figs. 3a–3c, respectively. Figure 3a indicates that, for $\bar{h}^* = 0.2$ to create a net propulsive force, the Reynolds number must be greater than 10^3 and the reduced frequency must be greater than 1.2. If the value of the amplitude is doubled, that is, for $\bar{h}^* = 0.4$, according to Fig. 3b, for the reduced frequency values greater than 0.5, net propulsive force is obtained even for a Reynolds number of 10^3. Furthermore, increasing the value of $\bar{h}^*$ to 0.6 gives a net propulsive force for a wide range of reduced frequencies, that is, $k > 0.3$, and Reynolds numbers, $Re > 10^3$, as shown Fig. 3c. Close examination of Figs. 3b and 3c indicate that when the amplitude is high, a 1 order-of-magnitude increase in Reynolds number, that is, from 10^4 to 10^5, has very little effect on the value of the propulsive force coefficient.

B. Airfoil with a Flexible Camber

The equation z_a for the time-dependent camber motion for the parabolic and flexible cambered thin airfoil is given by

Table 1 Averaged propulsive force coefficient c_T at $k = 0.4$ and $Re = 10^5$

$\bar{h}^*$	c_T, present	c_T, corrected	c_T, [13]	$\alpha_d = \alpha_s + \Delta\alpha$, deg	$\alpha_e = \tan^{-}(-\dot{h}/U_\infty)$, deg
0.8	−0.129	−0.119	−0.118	23	18
1.0	−0.205	−0.195	−0.176	23	21
1.2	−0.298	−0.288	−0.134	23	25

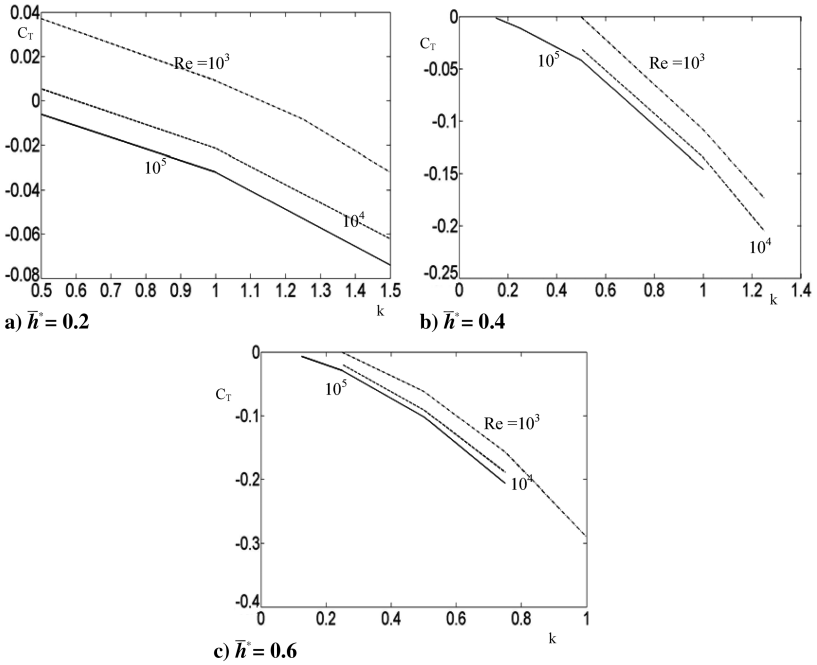

Fig. 3 Variation of the averaged propulsive force coefficient c_T with the reduced frequency k and the Reynolds number Re: a) $\bar{h}^* = 0.2$, b) $\bar{h}^* = 0.4$, and c) $\bar{h}^* = 0.6$.

$$z_a(x,t) = -a(t)x^2/b^2, \qquad a(t) = a^* \cos(\omega t), \qquad -1 \le x \le 1 \tag{21}$$

The sectional suction force coefficient is computed by Eq. (4), and the drag force coefficient is calculated again by the integration of the skin friction coefficient given by Eq. (11) along the upper and lower surfaces of the airfoil. The timewise variation of the suction force, drag force, and the net propulsive force coefficients are shown in Figs. 4a and 4b with respect to the varying Reynolds number and camber amplitude and the reduced frequency of the camber oscillation.

According to Figs. 4a and 4b, for a higher Reynolds number, camber magnitude, and reduced frequency, the averaged propulsive force coefficient is higher. For the low Reynolds number case, Fig. 4a, the suction force c_s barely overcomes the skin friction drag c_d to give an averaged propulsive force coefficient of $c_T = -0.0055$. The higher Reynolds number flow case, as shown in Fig. 4b, creates sufficient suction force to overcome the viscous effects to give an almost 1 order-of-magnitude higher propulsive force coefficient of $c_T = -0.0395$. A detailed inspection of Figs. 4a and 4b indicates that the viscous effects on the periodicity of the suction and the propulsive forces are very little whereas the viscous effects shift the propulsive force coefficients toward the positive side, which means it reduces the amplitude of the propulsive force.

Results of the parametric studies for the flexible cambered airfoil are shown in Figs. 5a and 5b as the variation of the propulsive force coefficient with respect to the varying dimensionless camber amplitude of $\bar{a}^* = a^*/b$, Reynolds number, and the reduced frequency k. Figure 5a indicates that, to have a propulsive force, the camber, based on the chord length, must be more than 5% even at a Reynolds number of 10^5 for the reduced frequency ranges between 1 and 2. According to the same figure, a 50% increase in camber amplitude can increase the propulsive force three- or fourfold for the same Reynolds number for the same reduced frequency range. Increasing the camber amplitude to 10%, Fig. 5b, doubles the propulsive force compared with the propulsive force obtained with Fig. 5a for $\bar{a}^* = 0.15$. Another interesting result shown in Fig. 5b is that, for a Reynolds number of 10^4 and $\bar{a}^* = 0.2$, the propulsive force increases almost linearly with respect to the reduced frequency.

The real positive effect of the flexible camber in forward flight is the delay of the flow separation by means of reducing the relative angle of attack [18] while lowering the camber properly, as shown in Fig. 1. In addition to affecting the overall performance of the flight, the flexible camber also contributes about 10% to the propulsive force, as shown in Figs. 4 and 5.

C. Heaving–Plunging Airfoil with a Flexible Camber

As the last case study, an airfoil with a flexible camber undergoing heaving–plunging motion is considered. The combined equation of

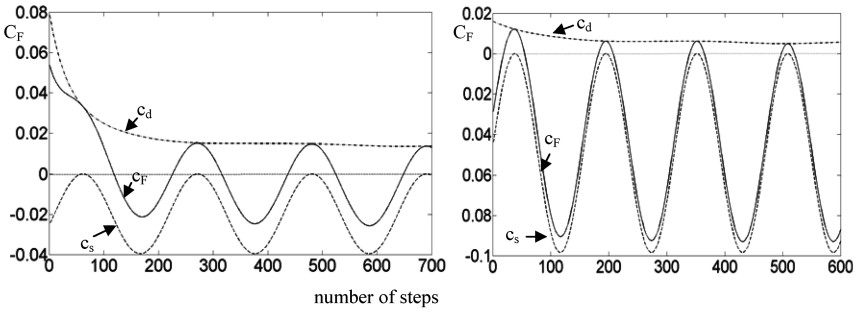

Fig. 4 Time variation of propulsive force coefficient $c_F = c_s + c_d$ for the flexible cambered airfoil: a) $Re = 10^4$, $\bar{a}^* = 0.15$, $k = 1.5$, $\Delta t = 0.01$; and b) $Re = 10^5$, $\bar{a}^* = 0.2$, $k = 2$, $\Delta t = 0.005$.

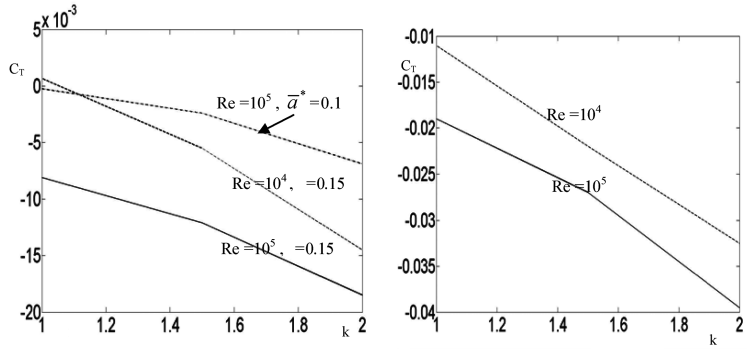

a) $\bar{a}^* = 0.1, 0.15$ b) $\bar{a}^* = 0.2$

Fig. 5 Variation of averaged propulsive force coefficient c_T for a flexible cambered airfoil: a) $\bar{a}^* = 0.1, 0.15$; and b) $\bar{a}^* = 0.2$.

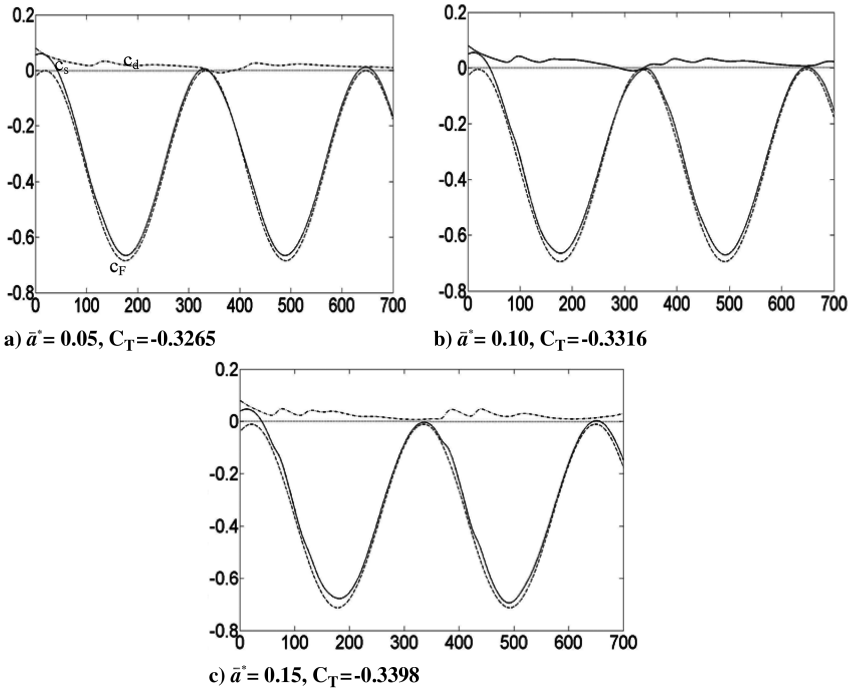

a) $\bar{a}^* = 0.05$, $C_T = -0.3265$ b) $\bar{a}^* = 0.10$, $C_T = -0.3316$

c) $\bar{a}^* = 0.15$, $C_T = -0.3398$

Fig. 6 Time variation of the propulsive force coefficients for heaving–plunging flexible airfoil at $Re = 10^4, k = 1$, and $\Delta t = 0.01$: a) $\bar{a}^* = 0.05$, b) =0.10, and c) =0.15.

motion is given as follows:

$$h = -h^* \cos(\omega t) \tag{22a}$$

and

$$z_a(x,t) = -a(t)x^2/b^2, \qquad a(t) = a^* \cos(\omega t + \pi/2) \qquad -1 \le x \le 1 \tag{22b}$$

As seen from Eqs. (22a) and (22b), there is a 90 deg phase lag between the heaving plunging and the time-dependent camber change. This provides us with an effective angle of attack that is less than the dynamic stall angle. The effective angle of attack for the combined motion is determined at the leading edge of the airfoil as follows:

$$\alpha_e = \tan^{-}[-(\dot{h} + w_{\text{aLE}})/U_\infty] \tag{23}$$

where w_{aLE} is the downwash at the leading edge caused by the time-dependent camber change.

Shown in Fig. 6 is the time variation of the force coefficient plots for the flexible airfoil at $Re = 10^4$ and $k = 1$ for three different maximum camber ratios: 1) $\bar{a}^* = 0.05$, 2) 0.1, and 3) 0.15. The corresponding averaged force coefficients are found as 1) $C_T = -0.3265$, 2) -0.3316, and 3) -0.3398, respectively. The ideal averaged force coefficients and the computed values are compared in Table 2 at associated effective angles of attack all less than the corresponding dynamic stall angle, which is 29 deg. According to Table 2, tripling the camber ratio from 5 to 15% results in only a 4% increase in the averaged force coefficient, that is, from -0.3265 to -0.3398. This shows that increasing the camber ratio

Table 2 Thrust coefficients for different $\bar{a}^*$ at $Re = 10^4$, $\bar{h}^* = 0.6$, and $k = 1$

$\bar{a}^*$	C_T	C_{Tid}	α_d, [11], deg	$\alpha_e = a\tan[-(\dot{h} + w_{\text{aLE}})/U_\infty]$, deg
0.05	−0.3265	−0.3433	29	27
0.10	−0.3316	−0.3505	29	23
0.15	−0.3398	−0.3625	29	18

does not produce a significant overall propulsive force increase for the case of a flexibly cambered airfoil undergoing heaving–plunging motion.

During all computations, the unsteady motion of the airfoil is started impulsively from rest. For the unsteady boundary-layer calculations, an equally spaced $2 \times 10 \times 10$ grid is employed. Usually, the step size $\Delta x = 0.1$ is kept constant. Depending on the value of the Reynolds number, Δy and Δt values are changed to 0.04, 0.01, and 0.005 for Reynolds numbers of 10^3, 10^4, and 10^5 respectively. Because the grid size is small, there is no need to be concerned about the memory requirements. Needless to say, the computational and data processing requirements are considerably small even on a PC compared with the CPU time and memory requirement using Navier–Stokes solvers. In particular, the estimates for CPU time requirements are very high for the flexible airfoil studies based on a moving–deforming grid.

VI. Conclusions

A method based on unsteady viscous–inviscid interaction is developed to determine the propulsive force generated by a flapping thin airfoil. The results are satisfactory, especially with the thickness correction, when compared with an existing similar study that implements a full Navier–Stokes solver. Because the boundary-layer approach is used here, the results obtained are meaningful before the occurrence of dynamic stall, which is delayed with the increase in reduced frequency.

The oscillatory pure camber change used here not only provides extra propulsive force for high Reynolds numbers and high amplitudes, but also prevents the flow separation by reducing the effective angle of attack.

The viscous effects obtained by the unsteady boundary-layer solution show very little alteration to the oscillatory behavior of the net propulsive force. They only reduce the amplitude of the leading-edge suction force obtained by the unsteady aerodynamic theory.

The study of the combined motion of a heaving–plunging airfoil with a periodically changing camber shows that the increase in the averaged propulsive force with the increase in maximum camber ratio is not so significant because the major contribution is due to heaving plunging. Therefore, it is possible to get sufficiently high propulsion with reasonable camber flexibility.

For future work, the aerodynamic efficiency and its optimization with respect to the maximum camber location for the heaving–plunging motion of a flexibly cambered airfoil can be studied with a constraint on the effective angle of attack to obtain higher propulsive forces without confronting dynamic stall.

Appendix: Unsteady Suction and Viscous Forces

The leading-edge suction force, the boundary-layer edge velocity, and the vorticity transport equation for an oscillating rigid and/or flexible thin airfoil are obtained using the quasi-unsteady aerodynamic approach as follows. The lifting pressure coefficient, c_{pa}, and the normalized perturbation velocity component in the x direction, u'/U, are related to each other by factor of 4 for the quasi-unsteady analysis in which the effect of the apparent mass term is neglected [19]. Using this fact for the simple harmonic motion of the thin airfoil whose equation is given by $z_a = z_a(x,t) = \bar{z}_a(x)e^{i\omega t}$, the approximate value of the amplitude of the edge perturbation velocity $\bar{u}'/U$ in terms of the amplitude of the lifting pressure $\bar{c}_{pa}$ reads as

$$\frac{\bar{u}'}{U} \cong \frac{\bar{c}_{pa}(x^*,k)}{4} = \frac{1}{\pi}\sqrt{\frac{1-x^*}{1+x^*}}\int_{-1}^{1}\sqrt{\frac{1+\xi^*}{1-\xi^*}}\frac{\bar{w}(\xi^*)\mathrm{d}\xi^*}{(x^*-\xi^*)U} + \frac{1}{\pi}[1-C(k)]\sqrt{\frac{1-x^*}{1+x^*}}\int_{-1}^{1}\sqrt{\frac{1+\xi^*}{1-\xi^*}}\frac{\bar{w}(\xi^*)\mathrm{d}\xi^*}{U} \tag{A1}$$

where k is the reduced frequency, and $\bar{w}(x) = i\omega\bar{z}_a + U\partial\bar{z}_a/\partial x$ is the amplitude of the downwash w. The corresponding time-dependent edge velocity then becomes

$$(U_e/U)(x,k,t) = 1 \pm (\bar{u}'/U)(x,k)e^{i\omega t} \tag{A2}$$

where $+$ corresponds to the upper and $-$ corresponds to the lower surfaces of the thin airfoil, respectively.

The leading-edge suction force S for an oscillating airfoil is given in [7] as follows:

$$S = -(\pi\rho P^2 + \alpha L) \tag{A3}$$

Here, L is the sectional lift, and α is the angle of attack. P, on the other hand, reads as

$$P = \lim_{x^*\to -1}\left(\tfrac{1}{2}\gamma_a\sqrt{x^*+1}\right) \tag{A4}$$

The relation between the surface vortex sheet strength γ_a and u' is given in [19] as $\gamma_a = 2u'$, where u' is provided by (A1). In Eq. (A3), the $-$ sign indicates that the propulsive force is against the freestream.

Using Eq. (A2), the boundary-layer edge velocity and, with Eqs. (A3) and (A4), the leading-edge suction force can be obtained for a flapping rigid and/or flexible airfoil.

I. Heaving–Plunging Thin Airfoil

The most general expression for the simple harmonic motion for this case will be given with real and imaginary parts as follows:

$$z_a(x,t) = h = h^* e^{i\omega t} = h^*(\cos\omega t + i\sin\omega t) \tag{A5}$$

The downwash expression $w = w(x,t)$ then reads

$$w(x,t) = \frac{\partial z_a}{\partial t} + U\frac{\partial z_a}{\partial t} = \dot{h} = i\omega h^* e^{i\omega t} \tag{A6}$$

After noting that the Theodorsen function $C(k) = F(k) + iG(k)$, the real part of P in Eq. (A4) becomes

$$P = -\sqrt{2}[F\sin\omega t + G\cos\omega t]\omega h^* \tag{A7}$$

which corresponds to the real part of h, that is, $h = h^*\cos\omega t$. Now, Eq. (A7) is used in Eq. (A3) to obtain the suction force.

Similarly, if we consider the real part of the motion and use Eq. (A6) as the downwash expression in Eq. (A1), after proper integrations [17,20], we get the boundary-layer edge velocity as follows:

$$U_e = U \pm [F\sin\omega t + G\cos\omega t]\omega h^*\sqrt{\frac{1-x^*}{1+x^*}} \tag{A8}$$

II. Flexible Thin Airfoil

Here, the camber of the airfoil is considered flexible so that the value of the maximum camber changes periodically by time. The equation of the camber line whose maximum camber is db distance away from the origin can be approximated by a cubic polynomial, as shown in Fig. A1.

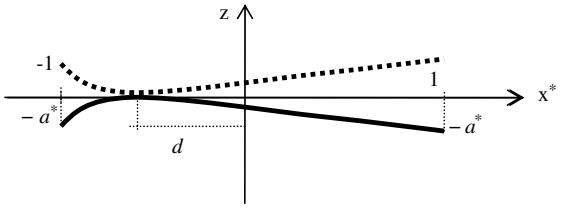

Fig. A1 Flexible camber line geometry for maximum camber of $a = -a^* \cos\omega t$

The equation of the camber line for Fig. A1 reads as

$$z_a(x,t) = a^* \cos\omega t\left[-\frac{2d}{(d^2-1)^2}\frac{x^3}{b^3}+\frac{3d^2-1}{(d^2-1)^2}\frac{x^2}{b^2} + \frac{2d}{(d^2-1)^2}\frac{x}{b}-\frac{3d^2-1}{(d^2-1)^2}-1\right] \tag{A9}$$

For the sake of simplicity, if a parabolically varying camber line is considered, then $d = 0$ gives

$$z_a(x,t) = -a^* \cos\omega t x^2/b^2 \tag{A10}$$

We can find the general expression for the vortex sheet strength and obtain the value of P with (A1). The real part of the resulting equation gives

$$P = \sqrt{2}[(FU/b - U/b - G\omega/2)\cos\omega t - (GU/b + F\omega/2)\sin\omega t]a^* \tag{A11}$$

Now, the boundary-layer edge velocity can be obtained by evaluating the integrals in Eq. (A1) to give

$$U_e = U \pm \{[(1+2x^*+F)U/b - G\omega/2]\cos\omega t - [(GU/b + (x^*+x^{*2}+F/2)\omega]\sin\omega t\}a^*\sqrt{\frac{1-x^*}{1+x^*}} \tag{A12}$$

These formulas can be cast into nondimensional forms using the definitions of reduced frequency $k = \omega b/U$ and reduced time $s = Ut/b$.

III. Boundary-Layer Equations for Flexible Camber

The velocity–vorticity formulation for the body-fixed coordinate system can be obtained for two-dimensional flows as follows. Let x–y be the noninertial body-fixed coordinate system attached to the body, as shown in Fig. A1. The continuity equation expressed in the noninertial frame of reference retains its form, and the horizontal, x, and vertical, y, momentum equations [21] for the u and v components of the velocity in their open forms read as

$$\frac{\partial u}{\partial t} + u\frac{\partial u}{\partial x} + v\frac{\partial u}{\partial y} = -\frac{\partial p}{\partial x} + \frac{1}{Re}\nabla^2 u + 2\Omega v - \Omega^2 x + \dot{\Omega} y \tag{A13a}$$

and

$$\frac{\partial v}{\partial t} + u\frac{\partial v}{\partial x} + v\frac{\partial v}{\partial y} = -\frac{\partial p}{\partial y} + \frac{1}{Re}\nabla^2 v - R'' - 2\Omega u + \Omega^2 y - \dot{\Omega} y \tag{A13b}$$

Here, Ω is the variable angular rotation due to the varying camber flexibility in the x direction, and R'' is the acceleration, only in the vertical direction for our problem, of the noninertial coordinate system with respect to a fixed coordinate system.

If we differentiate Eq. (A13a) with respect to y and (A13b) with respect to x, and subtract the former from the latter, we obtain

$$\frac{\partial \omega'}{\partial t} + u\frac{\partial \omega'}{\partial x} + v\frac{\partial \omega'}{\partial y} = \frac{1}{Re}\nabla^2\omega' - 2u\frac{\partial \Omega}{\partial x} + y\frac{\partial \Omega^2}{\partial x} - 2\dot{\Omega} - x\frac{\partial \dot{\Omega}}{\partial x} \tag{A14}$$

where $\omega' = \frac{\partial v}{\partial x} - \frac{\partial u}{\partial y}$ is the vorticity value expressed in the noninertial frame. We need the inertial frame vorticity, ω, to obtain the surface friction from the vorticity. The relation between the velocity vector $\mathbf{v}$ in the noninertial system and $\mathbf{V}$ in the inertial system reads as

$$\mathbf{v} = \mathbf{V} - \Omega\mathbf{k} \wedge (x\mathbf{i} + y\mathbf{j}) = \mathbf{V} + \Omega(y\mathbf{i} - x\mathbf{j}) \tag{A15}$$

where $\mathbf{i}$, $\mathbf{j}$, $\mathbf{k}$ are the unit vectors in the x, y, z directions, respectively. Applying the definition of vorticity, that is, $\boldsymbol{\omega} = \nabla \wedge \mathbf{v}$, to Eq. (A15) in the x–y coordinate system, the relation between the vorticity in the noninertial system and the inertial system becomes

$$\omega' = \omega - 2\Omega - x\frac{\partial \Omega}{\partial x} \tag{A16}$$

Substituting Eq. (A16) into Eq. (A14) gives

$$\frac{\partial \omega}{\partial t} + u\frac{\partial \omega}{\partial x} + v\frac{\partial \omega}{\partial y} = \frac{1}{Re}\nabla^2\omega - \frac{2}{Re}\nabla^2\left(\Omega + x\frac{\partial \Omega}{\partial x}\right) - y\frac{\partial \Omega^2}{\partial x} \tag{A17}$$

The boundary-layer assumption simplifies the first term and lets us omit the last term on the right-hand side of Eq. (A17). The second term on the right-hand side of Eq. (A17) vanishes for a parabolically cambered airfoil. The working equation in the boundary layer for the vorticity transport then becomes

$$\frac{\partial \omega}{\partial t} + u\frac{\partial \omega}{\partial x} + v\frac{\partial \omega}{\partial y} = \frac{1}{Re}\frac{\partial^2 \omega}{\partial^2 y} \tag{A18}$$

For the first-order approximation, the boundary-layer coordinate system s–n, with n measuring the normal distance to the surface and s measuring the distance along the boundary from the forward stagnation point, can be represented with x–y coordinates [14].

Acknowledgment

The help provided by Aydin Misirlioglu in developing and placing the graphs and the pictures in their proper places is greatly appreciated.

References

[1] Dawkins, R., *The Ancestor's Tale: A Pilgrimage to the Dawn of Life*, Orion Books, London, 2004, Chaps. 16, 26.

[2] Wang, Z. J., "Dissecting Insect Flight," *Annual Review of Fluid Mechanics*, Vol. 37, 2005, pp. 183–210. doi:10.1146/annurev.fluid.36.050802.121940

[3] Mueller, T. J., and DeLaurier, J. D., "Aerodynamics of Small Vehicles," *Annual Review of Fluid Mechanics*, Vol. 35, 2003, pp. 89–111. doi:10.1146/annurev.fluid.35.101101.161102

[4] Platzer, M. F., Jones, K. D., Young, J., and Lai, C. S., "Flapping-Wing Aerodynamics: Progress and Challenges," *AIAA Journal*, Vol. 46, No. 9, 2008, pp. 2136–2149. doi:10.2514/1.29263

[5] Milne-Thomson, L. M., *Theoretical Aerodynamics*, 4th ed., Dover, New York, 1973, Chap. 5.

[6] von Karman, T., and Burgers, J. M., "General Aerodynamics Theory—Perfect Fluids," *Aerodynamic Theory*, Vol. 2, edited by W. F. Durand, Julius Springer, Berlin, 1935, pp. 301–310.

[7] Garrick, I. E., "Propulsion of a Flapping and Oscillating Airfoil," NACA TR-567, 1936.

[8] Theodorsen, T., "General Theory of Aerodynamic Instability and the Mechanism of Flutter," NACA TR-496, 1935.

[9] Gulcat, U., "Separate Numerical Treatment of Attached and Detached Flow Regions in General Viscous Flows," Ph.D. Dissertation, School of Aerospace Engineering, Georgia Inst. of Technology, Atlanta, GA, 1981.

[10] Wu, J. C., Wang, C. M., and Gulcat, U., "Zonal Solutions of Unsteady Viscous Flow Problems," AIAA Paper 84-1637, 1984.

[11] Abbot, I. H., and von Doenhoff, A. E., *Theory of Wing Sections*, 1st ed., Dover, New York, 1959, Chap. 7.

[12] Prouty, R. W., *Helicopter Performance Stability and Control*, Krieger, Malabar, FL, 1995, Chap. 6.

[13] Tuncer, I. H., and Platzer, M. F., "Computational Study of Flapping Airfoil Aerodynamics," *Journal of Aircraft*, Vol. 37, No. 3, 2000, pp. 514–520. doi:10.2514/2.2628

[14] Schlichting, H., *Boundary-Layer Theory*, 6th ed., McGraw–Hill, New York, 1968, Chap. 7.

[15] Sankar, N. L., "Numerical Study of Laminar Unsteady Flow Over Airfoils," Ph.D. Dissertation, School of Aerospace Engineering, Georgia Inst. of Technology, Atlanta, GA, 1977.

[16] Press, W. H., Flannery, B. P., Teukolsky, S. A., and Vetterling, W. T., *Numerical Recipes*, Cambridge Univ. Press, London, 1992, Chap. 2.

[17] Van Dyke, M. D., "Second-Order Subsonic Airfoil Theory Including Edge Effects," NACA TR-1274, 1956.
[18] Shyy, W., Berg, M., and Ljungqvist, D., "Flapping and Flexible Wings for Biological and Micro Air Vehicles," *Progress in Aerospace Sciences*, Vol. 35, No. 5, 1999, pp. 455–505. doi:10.1016/S0376-0421(98)00016-5
[19] Bisbilinghof, R. L., Ashley, H., and Halfman, R. L., *Aeroelasticity*, Dover, New York, 1996, Chap. 5.
[20] Katz, J., and Plotkin, A., *Low-Speed Aerodynamics*, McGraw–Hill, New York, 1991, Apps. A, B.
[21] Shames, I. H., *Mechanics of Fluids*, McGraw–Hill, New York, 1962, Chap. 5.